# Present Status of Wave Forecasting at E.C.M.W.F.

**Jean-Raymond Bidlot**

*ECMWF, Shinfield Park, Reading*
*RG2 9AX, United Kingdom*
*jean.bidlot@ecmwf.int*

**ABSTRACT**

The key features of the current operational wave model used by ECMWF are described.

## 1 Introduction

ECMWF produces twice daily analyses and forecasts of the sea state over the world oceans. The physics of the wave model is based on WAM Cycle 4 (Komen et. al (1994)). The ever changing operational environment required further developments to be incorporated in the wave model. Furthermore, there were numerical improvements in the advection scheme, in the time-integration scheme and in the determination of the wave stress. The parametrisation used for the wind input source term and the dissipation were also adapted. The WAM code was originally written for global scale applications, however, it was extended to also run on smaller domains and in shallower water. We refer to this version of model as 'ECWAM'.

In its current global configuration, ECWAM is two-way coupled to the atmospheric model and altimeter wave height data are assimilated to produce the wave analysis (Janssen (2004)). It is run in all forecasting systems in use at ECMWF, from deterministic and probabilistic medium range forecasts, to monthly and seasonal time scales. It is also run operationally as a stand alone model for all the Seas around Europe at a slightly higher horizontal resolution. This configuration also includes effects of surface currents. The surface currents are from the TOPAZ4 system as disseminated by the Norwegian Meteorological Institute under the MyOcean project. A detailed description of ECWAM is periodically updated on the web as part of the documentation of ECMWF Integrated Forecasting System (IFS) (http://www.ecmwf.int/research/ifsdocs/).

## 2 Present status

This section summarises the key components of ECWAM. The code was updated in operations on June 19th, 2012 as part of the implementation of the new model cycle (CY38R1).

### 2.1 Wind input source term

The input source term $S_{\text{in}}$ of ECWAM is given by

$$S_{\text{in}} = \gamma N \tag{1}$$

where $\gamma$ is the growth rate and $N$ is the action density spectrum.

Following the adaptation of Miles critical layer theory by Janssen (1991), $\gamma$ can be written as

$$\frac{\gamma}{\omega} = \varepsilon \frac{\beta_{\max}}{\kappa^2} \exp(Z)\, Z^4 \left( \frac{u_*}{c} \max(\cos(\theta-\phi),0) \right)^2, \quad Z \leq 0 \tag{2}$$

where $\omega$ is the angular frequency, $\varepsilon$ the air–water density ratio, $\kappa$ the von Kármán constant ($\kappa$=0.4) and $\beta_{\rm m}$ a constant . As usual, $u_*$ denotes the friction velocity, $c$ the phase speed of the waves, $\phi$ the wind direction and $\theta$ the direction in which the waves propagate. Z is the effective wave age parameter:

$$Z = \ln\left(\frac{g z_0}{c^2}\right) + \frac{\kappa}{\cos(\theta-\phi)(\frac{u_*}{c}+z_\alpha)} \tag{3}$$

where g is the acceleration of gravity, $z_0$ the roughness length and $z_\alpha$ is the wave age tuning parameter.

As follows from the expression of the growth rate of waves by wind, the ECWAM is based on friction velocity scaling. Therefore, the friction velocity $u_*$ is required. In the practice of ocean wave modelling the friction velocity is not readily available, but surface winds at 10m height are available. In the original version of the WAM model, the friction velocity was then obtained by assuming that the relation between $u_*$ and the wind speed at a given height ($U(z)$) is given by the logarithmic profile.

$$U(10m) = \frac{u_*}{\kappa} \ln\left(\frac{10}{z_0}\right) \tag{4}$$

This assumes neutral stable conditions, which is only approximately correct. A proper solution is to transform the surface winds into their neutral wind counterparts. When coupled to the atmospheric model, this transformation can easily be achieved by using the atmospheric model surface stress and the logarithmic wind profile with the roughness length based on the Charnock relation:

$$z_0 = \frac{\hat{\alpha} u_*^2}{g\sqrt{1-y}}, \quad y = \tau_{\rm w}/u_*^2 \tag{5}$$

$\tau_{\rm w}$ is the stress induced by gravity waves (the "wave stress")

$$\tau_{\rm w} = \frac{g}{\varepsilon} \int {\rm d}\omega\, {\rm d}\theta\, S_{\rm in} \vec{k} \tag{6}$$

In (6) the frequency integral extends to infinity, but in its evaluation only a diagnostic $f^{-5}$ tail of gravity waves is included above a cut-off prognostic frequency (see below) and the higher level of capillary waves is treated as a background small-scale roughness.

As in the original WAM, $\beta_{\max}$=1.2, but with this latest cycle, $z_\alpha$ was reduced to 0.008 (from 0.011) with $\hat{\alpha}$=0.006. The reduction was motivated by the known tendency of the model to generate too much waves at low frequencies. As seen in Fig. 1, the new value of $z_\alpha$ reduces the wind input of long waves. The dissipation source function was adapted accordingly as described below. Note that this small adjustment of $z_\alpha$ still fits the observational data used by Janssen to develop his formulation (Janssen (1991)).

## 2.2 Damping of long waves

The Miles critical layer theory is, to some extent, an idealization of reality because effects of turbulent eddies on wave growth have not been taken into account. The classical eddy viscosity model is based on the assumption that air-turbulence is the fastest process, much faster than the typical period of the ocean waves. This assumption is however not valid for swells which have propagation speeds that are much faster than a typical wind speed scale $V = U(z = L)$ where $L = 1/k$ with $k$ the wavenumber. In those circumstances momentum transport by turbulent eddies is much less effective. A more quantitative

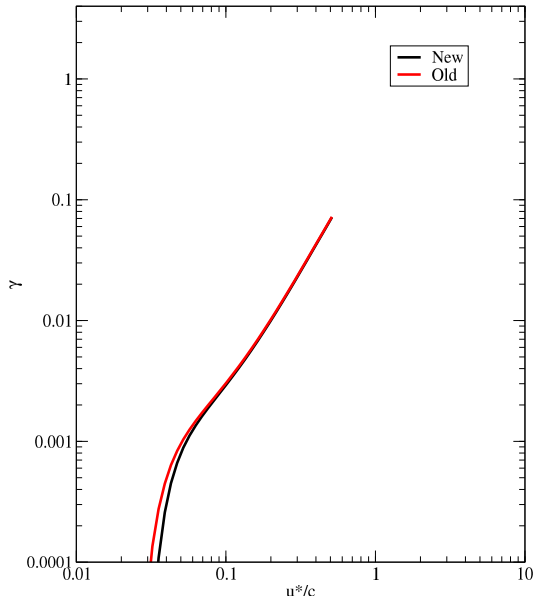


*Figure 1: Non dimensional growth rate $\gamma/f$ for a Charnock parameter $\alpha_{\rm CH} = 0.0144$. New (black) is for $z_\alpha = 0.008$ and old (red) for $z_\alpha = 0.011$.*

discussion of the truncation of transport by turbulent eddies is given in Janssen (2004). An asymptotic analysis of the resulting boundary value problem (i.e. including the small effects of turbulent eddies) then allows to obtain the following expression for the growth rate.

$$\frac{\gamma}{\omega} = \varepsilon \left\{ \frac{\beta_{\max}}{\kappa^2} \exp(Z)\, Z^4 \left( \frac{u_*}{c} \max(\cos(\theta-\phi),0) \right)^2 + 2\kappa \left( \frac{u_*}{c} \right)^2 \left( \cos(\theta-\phi) - \frac{c}{V} \right) \right\}, \quad Z \le 0 \quad (7)$$

The first term on the right-hand side then corresponds to the Miles critical layer effect (cf. Eq. 2), while the second term gives a normally small correction to the growth rate due to air turbulence. Nevertheless this small correction gives important effects for swells propagating over large distances as happens for instance for ocean generated by extra-tropical storms which propagate towards the East Tropical Pacific. Typical damping scales according to (7) are of the order of thousands of kilometres. For waves propagating with the wind a plot of the Miles parameter $\beta$ as function of the dimensionless phase speed $c/u_*$ is given in Fig. 2. In order to appreciate the effects of growth/damping due to air turbulence the second term of Eq. (7) is plotted separately for two different wave propagation angles namely, with and against the wind. The plot shows that when $c > V\cos(\theta-\phi)$ the waves are damped, but, clearly, compared to the growth rate of the short waves the damping rates are small. The damping formulation was implemented in the operational system in September 2009 (CY35R3).

## 2.3 Wind gustiness

The input source term given in (1) and (2) assumes homogeneous and steady wind velocity within a model grid-box and during a time-step. Assuming that the wind speed variations with scales much larger than both the spatial resolution and the time step are already resolved by the atmospheric model, we need to include the impact of the wind variability at scales comparable to or lower than the model resolution (wind gustiness). To achieve this, an enhanced input source term with the mean impact of gustiness can be estimated as (Abdalla and Cavaleri (2002))

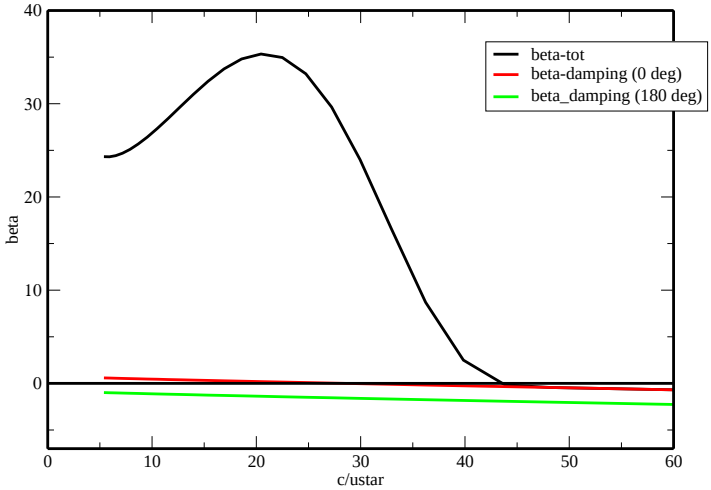


*Figure 2: The Miles parameter $\beta$ as function of $c/u_*$ for waves propagating in the wind direction. The effect of air turbulence on the growth rate for two different propagation directions is shown as well. ($\beta = \frac{\beta_{\max}}{\kappa^2}\ \exp(Z)\ Z^4$)*

$$\overline{\gamma}(u_*) = \frac{1}{\sigma_*\sqrt{2\pi}} \int_{-\infty}^{\infty} \exp\left\{-\frac{(u_* - \overline{u}_*)^2}{2\sigma_*^2}\right\} \gamma(u_*) \mathrm{d}u_* \tag{8}$$

where $u_*$ represents the instantaneous (unresolved) wind friction velocity, $\sigma_*$ is the standard deviation of the friction velocity and the over-barred quantity represents the mean value of the quantity over the whole grid-box/time-step. Note that this mean value is the (gust-free) value obtained from the atmospheric model. The integral above can be approximated using the Gauss-Hermite quadrature as

$$\overline{\gamma}(u_*) = 0.5\,[\gamma(\overline{u}_* + \sigma_*) + \gamma(\overline{u}_* - \sigma_*)] \tag{9}$$

The magnitude of variability can be represented by the standard deviation of the wind speed. To estimate the standard deviation of the wind speed, one can use the empirical expression proposed by Panofsky (1991) which can be written as

$$\frac{\sigma_{10}}{u_*} = \left\{ b_{\mathrm{g}} + \frac{1}{2}\left(\frac{z_i}{-L}\right)\right\}^{1/3} \tag{10}$$

where $\sigma_{10}$ is the standard deviation of the 10 m wind speed ($U_10$), $z_i$ is the height of the lowest inversion, $L$ is the Monin-Obukhov length, and $b_{\mathrm{g}}$ is a constant representing the background gustiness level that exists at all times irrespective of the stability conditions. The quantity $z_i/L$, which is a measure for the atmospheric stability, is readily available from the atmospheric model. In order to use (10) to derive $\sigma_*$, we use the following expression for the drag coefficient $C_{\mathrm{d}}$ in terms of 10m wind speed $U_{10}$

$$C_{\mathrm{d}} = a + b\,U_{10}, \quad a = 0.810^{-3}, \quad b = 0.0810^{-3}, \quad u_* = \sqrt{C_{\mathrm{d}}}\,U_{10} \tag{11}$$

which yields

$$\sigma_* = \frac{1}{U_{10}}\left\{1 + \frac{0.5\,b\,U_{10}}{C_{\mathrm{d}}}\right\}\left\{b_g\,u_*^3 + \frac{1}{2}\,\kappa\,w_*^3)\right\}^{1/3} \tag{12}$$

where $w_*$ is the free convection velocity scale which is obtained from the atmospheric model

$$w_* = u_*\left\{\frac{1}{\kappa}\left(\frac{z_i}{-L}\right)\right\}^{1/3} \quad for\ L < 0 \quad and \quad w_* = 0 \quad for\ L >= 0 \tag{13}$$

Note that the impact of the background level of gustiness is assumed to be implicitly included in the parametrisations of the atmospheric model as well as in the wave model. Therefore, $b_g$ is set to 0.

### 2.4 Air density

The growth rate of waves is proportional to the ratio of air to water density, $\varepsilon$, as can be seen in (2). Under normal conditions, seawater density varies within a very narrow range and, therefore, it can be assumed to be constant. On the other hand, air density has a wider variability. Based on basic thermodynamic concepts, it is possible to compute the air density using the formula

$$\rho_{air} = \frac{P}{RT_v} \tag{14}$$

where $P$ is the atmospheric pressure, $R \simeq 287.04$ J kg$^{-1}$ K$^{-1}$ is a constant defined as $R = R_+/m_a$, with $R_+$ the universal gas constant ($R_+ \simeq 8314.36$ J kmol$^{-1}$ K$^{-1}$) and $m_a$ is the molecular weight of the dry air ($\simeq 28.966$ kg kmol$^{-1}$), and $T_v$ is the virtual temperature. The virtual temperature can be related to the actual air temperature, $T$, and the specific humidity, $q$, by: $T_v \simeq (1+0.6078q)T$ . In particular, the surface pressure is used for $P$, the skin temperature is used for $T$, and the humidity at 2m height is used for $q$.

Both gustiness and air density effected were added to the operational system in April 2002 (CY25R2).

### 2.5 Wave dissipation

With the change of $z_\alpha$ in (3) in the latest model cycle, the wave dissipation source function had to be adjusted, still keeping the modified WAM cycle 4 formulation as described in Bidlot et. al (2007) but with adequate coefficients.

$$S_{\rm ds} = -C_{\rm ds} \langle\omega\rangle \left(\langle k\rangle^2 m_0\right)^2 \left[(1-\delta)\frac{k}{\langle k\rangle} + \delta\left(\frac{k}{\langle k\rangle}\right)^2\right] N \tag{15}$$

with

$$C_{\rm ds} = 1.33,\ \delta = 0.5 \tag{16}$$

where $m_0$ is the total wave variance per square metre, $k$ the wavenumber, and $\langle\omega\rangle$ and $\langle k\rangle$ are the mean angular frequency and mean wavenumber, respectively.

The mean wave number $\langle k\rangle$ and mean frequency $\langle\omega\rangle$ are defined using weighted spectral integrals that put more emphasis on the high frequencies. The mean angular frequency $\langle\omega\rangle$ is defined by means of the first $\omega$-moment of the spectrum

$$\langle\omega\rangle = \frac{\int d\vec{k}\ \omega F(\vec{k})}{\int d\vec{k}\ F(\vec{k})} \tag{17}$$

A similar relation for the mean wavenumber $\langle k\rangle$ is also used

$$\sqrt{\langle k\rangle} = \frac{\int d\vec{k}\ \sqrt{k} F(\vec{k})}{\int d\vec{k}\ F(\vec{k})} \tag{18}$$

### 2.6 Nonlinear transfer

The calculation of the non linear source term in deep waters is still based on the Discrete Interaction Approximation (DIA). For shallow waters, the non linear transfer coefficients are rescaled.

$$Tranfer_{nl}(shallow) = f(k,h) Transfer_{nl}(deep) \tag{19}$$

with $k$ the wavenumber, and $h$ the water depth.

Following Janssen and Onorato (2007), using the narrow band approximation, it was shown that the scaling factor $f(k,h)$ could be written as

$$f(k,h) = \frac{R^2}{T^8 \frac{\partial v_g}{\partial k}} \tag{20}$$

where

$$\frac{\partial v_g}{\partial k} = \left\{ T - kh\left(1-T^2\right) \right\}^2 + 4(kh)^2 T^2 \left(1-T^2\right). \tag{21}$$

$$R = \frac{9T^4 - 10T^2 + 9}{8T^3} - \frac{1}{kh}\left\{ \frac{(2v_g - c/2)^2}{c_S^2 - v_g^2} + 1 \right\}. \tag{22}$$

$$T = \tanh(kh),\ v_g = \frac{1}{2}c\left\{ 1 + \frac{2kh}{\sinh(2kh)} \right\},\ c = \frac{\omega}{k},\ c_S = \sqrt{gh},\ \omega = \sqrt{gkT} \tag{23}$$

This scaling factor will give rise to a reduction of the strength of the nonlinear transfer around $kh = 1.363$, which has consequences for the frequency downshift of the spectrum in shallow waters. Note that for very shallow water, the scaling factor can become, very large. In the current implementation, we have limited its value. Namely,

$$f(k,h) = \min(f(k,h), 10) \tag{24}$$

This shallow water scaling was implemented in June 2008 (CY33R1).

Note that since May 2011 (CY37R2), a second order correction to the computed first order wave spectrum is applied in the post-processing of all integrated output parameters. The consequence of that change is mostly limited to shallow waters. Refer to the online documentation for further details.

## 2.7 Bottom effects

Bottom friction source term is still based on the WAM cycle 4 formulation

$$S_{\text{bot}} = -2\, C_{\text{bot}}\, \frac{k}{\sinh(2kh)} N \tag{25}$$

where the constant $C_{\text{bot}} = 0.038/g$

The bottom induced wave breaking source term of Battjes and Janssen (1978) was introduced to account for the extra dissipation due to breaking waves over very shallow depths.

## 2.8 Diagnostic tail and growth limiter

When solving the energy balance equation, the wave model spectrum $F(f,\theta)$ is discretized between a minimum ($f_{min}$) and maximum frequency ($f_{max}$), however, because of limitations due to the numerics and the assumptions made on the model source terms, the equations are only integrated up to a cut-off prognostic frequency. For frequencies above this cut-off frequency, ECWAM enforces a diagnostic $f^{-5}$ spectral shape ($\frac{k^{-3}}{v_g}$ in shallow waters).

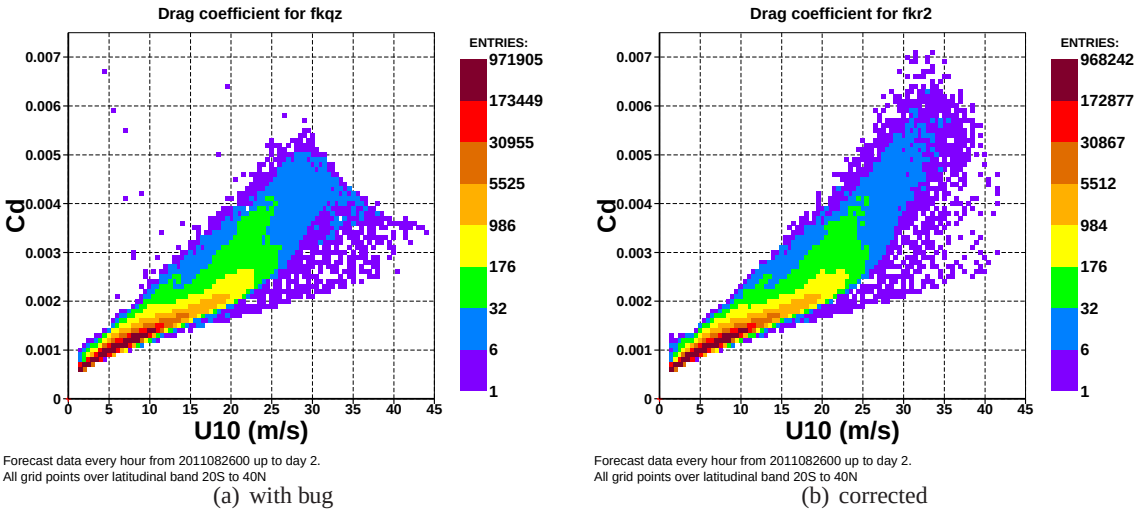


(a) with bug (b) corrected

*Figure 3: Drag coefficient and corresponding 10m wind speed for all model grid points between 20°S and 40°N for a high resolution coupled atmosphere-ECWAM forecast from 26 August 2011, 0 UTC, output every hour for 2 days. Left pane: the incorrect stress table was used. Right panel: the correct stress table was used.*

$$f_{min} \leq f \leq \min(2.5\, f_{meanWS}, f_{max}) \tag{26}$$

where $f_{meanWS}$ is the mean frequency based on the $\omega^{-1}$ moment but only for spectral components for which the wind input source term is positive.

The source terms are integrated forward in time using a fully implicit scheme (Hersbach and Janssen (1999)). Because of the limitations of that scheme, a growth limitation needs to be imposed. In ECWAM, a variant of the growth limiter of Hersbach and Janssen (1999) is used: the maximum increment in the spectrum, $|\Delta F|_{\max}$, is given by

$$|\Delta F|_{\max} = 3 \times 10^{-7} g u_* f^{-4} f_{meanWS}\, \Delta t \tag{27}$$

## 2.9 Surface stress calculation

The resolution and accuracy of the total stress and wave induced stress tables used by WAM have been enhanced a few times in ECWAM, but in April 2005 (CY29R1), a bug in the determination of the total surface stress was introduced, such that stresses for high winds ($\geq 30 m/s$) were artificially capped. As a consequence, the relation between drag coefficient ($C_{\rm d}$) and 10m wind speed ($U_{10}$) showed an apparent limit for high winds (Fig.3, left panel) and a few unrealistic outliers for low winds. When the bug is corrected, the artificial limit disappears as well as the odd values of $C_d$ at low wind speeds (Fig.3, right panel). This bug fix was implemented in the latest model cycle. Note that it is has been reported that the values of the drag coefficient might tail off for large winds (Doyle et al. (2012), Holthuijsen et al. (2012)). It should however not be achieved by artificially capping the drag coefficient as was unintentionally done prior to the bug fix. The behaviour of waves under extreme winds is a topic of further research.

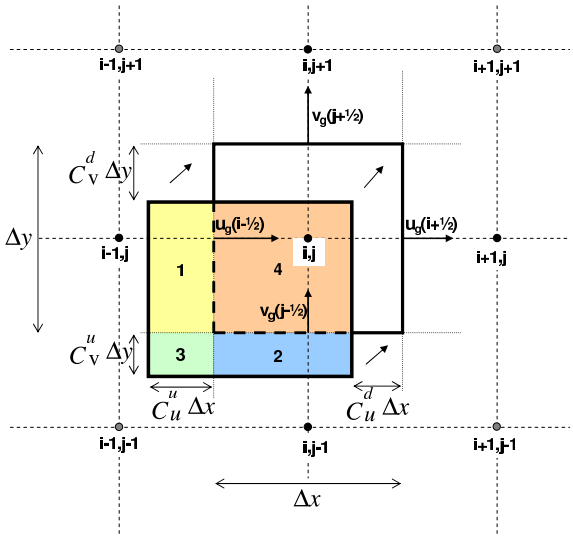


*Figure 4: Schematic representation of the volumes swept in the corner transport method.*

## 2.10 Grid and advection scheme

As for the advection scheme, the original first order upwinding scheme was improved by considering the corner points as well. For the simple case of the advection in x,y space. The wave energy balance equation in flux form becomes

$$\frac{\partial}{\partial t}F + \frac{\partial}{\partial x}(u_g F) + \frac{\partial}{\partial y}(v_g F) = 0, \tag{28}$$

where $F$ is the wave variance spectrum and ($u_g$,$v_g$) are the group speed $x$ and $y$- components.

One of the drawbacks of using the first order upwinding scheme is that it only considers contributions from neighbouring grid points in the $x$ and $y$ directions, no contributions from the corners of the grid are considered. The scheme can be extended to account for the corner points by using the Corner Transport Upstream (CTU) scheme. One way to understand how the CTU algorithm works is to follow how a grid box cell, centred at point $(i, j)$ is advected backwards over one time step by the group speed velocities on each grid box facet ($u_g(i \pm 1/2)$, $v_g(j \pm 1/2)$) (Fig.4).

$$u_g(i \pm 1/2) = \frac{u_g(i) + u_g(i \pm 1)}{2},\ v_g(j \pm 1/2) = \frac{v_g(j) + v_g(j \pm 1)}{2}. \tag{29}$$

Following the location of the gridbox at time level $n+1$ back in time, one gets the picture in Fig.4, where the transported cell overlaps on three upstream cells. The area of intersections represents the weights to attribute to $F$ on the original grid but at the previous time level $n$. The scheme can then be written as:

$$F_{i,j}^{n+1} = (1-C_u^d)(1-C_v^d)F_{i,j}^n + C_u^u(1-C_v^d)F_{i-1,j}^n + C_v^u(1-C_u^d)F_{i,j-1}^n + C_u^u C_v^u F_{i-1,j-1}^n \tag{30}$$

where the Courant numbers in $x$ and $y$ directions are

$$\begin{aligned} C_u^u &= \frac{u_g(i-1/2)\Delta t}{\Delta x},\ C_v^u = \frac{v_g(j-1/2)\Delta t}{\Delta y}, \\ C_u^d &= \frac{u_g(i+1/2)\Delta t}{\Delta x},\ C_v^d = \frac{v_g(j+1/2)\Delta t}{\Delta y}. \end{aligned} \tag{31}$$

As in the upwinding scheme, stability is conditional on all Courant numbers to be between 0 and 1. This scheme was generalised for spherical coordinates and for irregular lat-lon grid as used in operations.

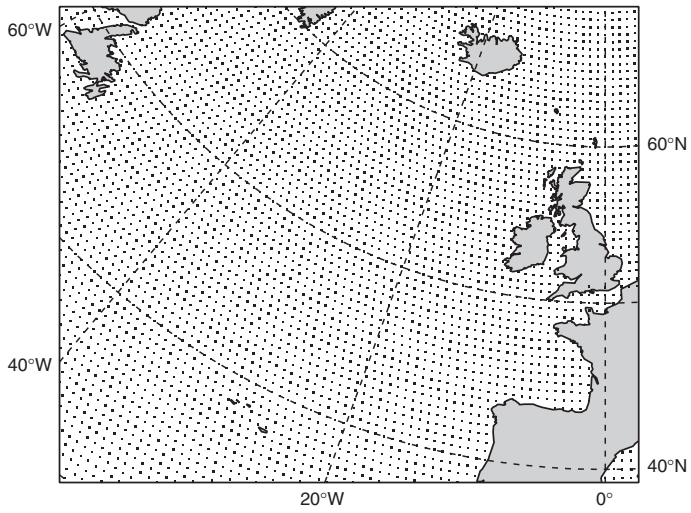


*Figure 5: Irregular grid for North Atlantic area on a polar stereographic projection.*

When moving towards the poles, the distance in the latitudinal direction decreases. Clearly, close to the poles, violation of the CFL criterion occurs. In ECWAM, this problem was solved by choosing an irregular spherical grid in such a way that the distance between grid points along each latitude is more or less fixed to its value at the equator (the latitudes themselved are equally spaced). An example for such a grid is shown in Fig.5. The advection scheme is still formulated in terms of spherical coordinates but the gradient in the longitudinal fluxes is evaluated by linear interpolation of the fluxes from the closest neighbours. The additional advantages of the use of an irregular spherical grid is a reduction in the total number of grid points by 30%, giving a substantial reduction in the cpu consumption.

Finally, the wave model grid has been extended up to the North pole. The singularity at the North pole is avoided by allowing a slight offset of the latitude from $90^o$ and the pole itself is represented by 2 grid points.

## 2.11 Parametrization of subgrid bathymetry

The top panel of Fig. 6 shows the bathymetry for an area centred on the Tuamotu Archipelago in the South Pacific as derived from the ETOPO2 data (only sea points with water depth less than 300 m are shown). The complexity of the bathymetry is clearly visible. This data set can be used to produce the wave model grid by averaging the depths of all ETOPO2 sea points within a model grid box and vice-versa for land points. A model grid box is considered to be over sea if more than half the ETOPO2 points are sea points and a small area 4 by 4 minutes centred on the model grid point is not land. Fig.6 shows the resulting mean depth for the 55 km grid (middle panel). Much of the shallow features of the archipelago are gone. It is therefore not surprising that, when modelling swell propagation across this area, very little attenuation is experienced.

Based on a similar idea as in Tolman (2003) and Hardy et al. (2001), we have modified the wave propagation scheme to limit the amount of wave energy that can be advected through these sub grid bathymetric features (see documentation for details).

The total obstruction for each upwind flux is then obtained by summing over all lines that are intersecting the corresponding grid box facet. High frequency waves are less affected by the bathymetry than low frequency components. Thus, at each grid point there is a transmission factor for each discretised frequency bin corresponding to all four cardinal directions. The bottome panel of Fig.6 shows how much energy is allowed to propagate towards the north for the first frequency bin of the model (wavelength

1360 m). These long waves will indeed be quite attenuated as they cross the Archipelago. On the other hands, the short waves should be a lot less affected by the unresolved bathymetry (not shown).

This simple scheme was implemented in operations in March 2004.

### 2.12 Data assimilation

Data assimilation is currently only performed with altimeter wave height observations, using an adaptation of the original Optimum Interpolation scheme introduced by Lionello et al. (1992).

Generally the impact of assimilating altimeter data is still beneficial, albeit, very limited in the forecast (Fig.7).

## 3 Impact of latest operational change

The latest change to the input/dissipation source terms had a very positive impact on the quality of wave data. At ECMWF, all contributions that are part of a new cycle are combined and rigorously tested in a pre-operational environment (e-suite) that can be compared to the operational products (o-suite). The improved quality of the e-suite wave model spectra at analysis time is clearly visible in Fig. 8. The tendency to over-estimate wave energy for periods above 12 seconds has been removed without any deteriorations of the shorter waves. A similar picture emerges when looking at the forecasts for significant wave height, peak period (Fig. 9) when compared to in-situ observations. Note that the improvement for wind speeds was not so marked. A similar comparison with altimeter wave heights yields similar improvement for the e-suite in all areas (Fig. 10).

## 4 Conclusions

Since the last Wave Workshop, the ECMWF forecasting system, including the waves, has seen remarkable improvement in the quality of its products. This paper summarises the key elements of the wave model as currently implemented in the operational system. It is by no means the end of its developments. It is hoped that in the coming years, we will be able to carry to operations some of the latest developments in numerics, source term parametrisations and further integration with the ocean, the sea ice and the atmosphere.

## Acknowledgements

The work and dedication of all past and present colleagues at ECMWF is kindly acknowledged. Their collective efforts have yielded an unprecedented success in all aspects of weather prediction with benefts to an ever increasing number of users.

## References

Abdalla, S., and L. Cavaleri, 2002. Effect of wind variability and variable air density on wave modeling. *J. Geophys. Res.*, **107**, 3080, doi:10.1029/2000JC000639.

Battjes, J.A. and J.P.F.M. Janssen, 1978. Energy loss and set-up due to breaking of random waves, Proceedings Coastal Engineering. ASCE, pp. 569-587.

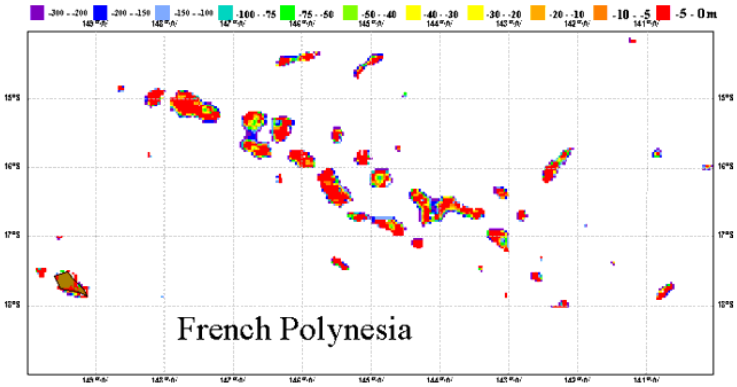


(a) ETOPO2

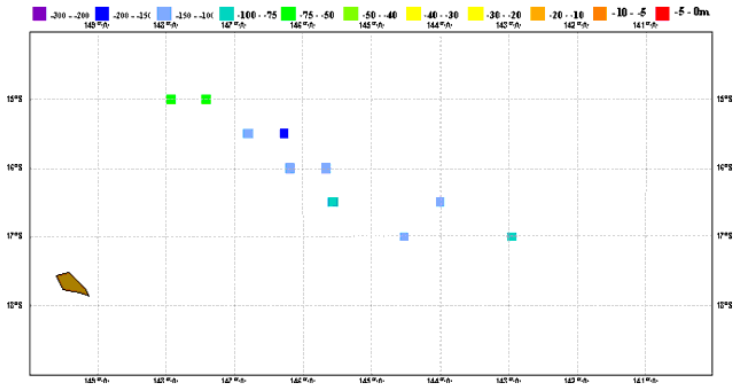

(b) WAM bathymetry

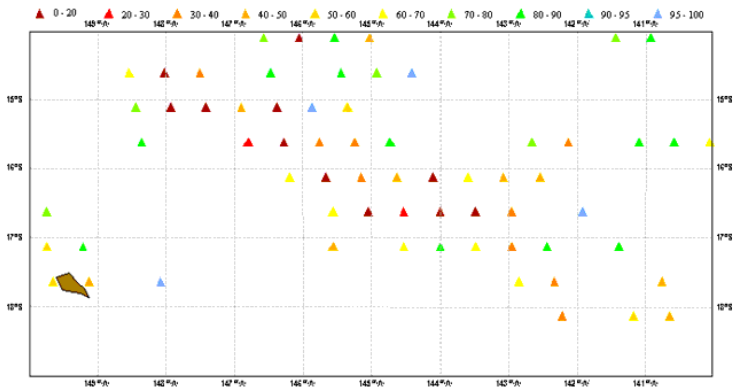

(c) Obstructions

*Figure 6: Top panel: ETOPO2 bathymetry obtained from the National Geophysical Data Center (only sea points shallower than 300 m are shown). Middle panel: WAM bathymetry (only sea points shallower than 300 m are shown) for the 55 km grid. Bottom panel: Percentage of the wave energy that is allowed to propagate northwards for the lowest frequency bin (0.035 Hz).*

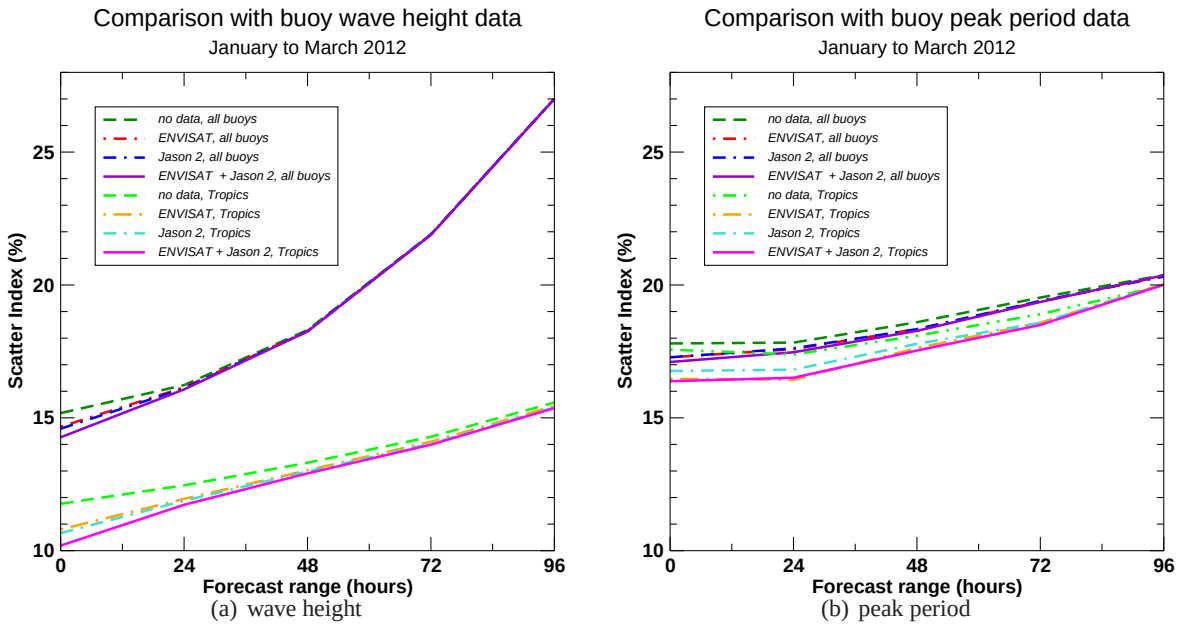


(a) wave height (b) peak period

*Figure 7: Impact of using altimeter wave height data in a comparison against all available buoy data and all buoy data from the Tropics for wave height (left panel) and peak period (right panel). A set of 3 months stand alone runs at 28 km resolution, forced by operational analysis winds were performed: a reference run with no data, one with ENVISAT data, another one with Jason 2 data and a final run with both ENVISAT and Jason 2 data. The buoy data are similar to the one used for the JCOMM Wave Forecast Verification Project (Bidlot et. al (2007)). Scattex Index is the standard deviation of the difference normalised by the mean of the observations.*

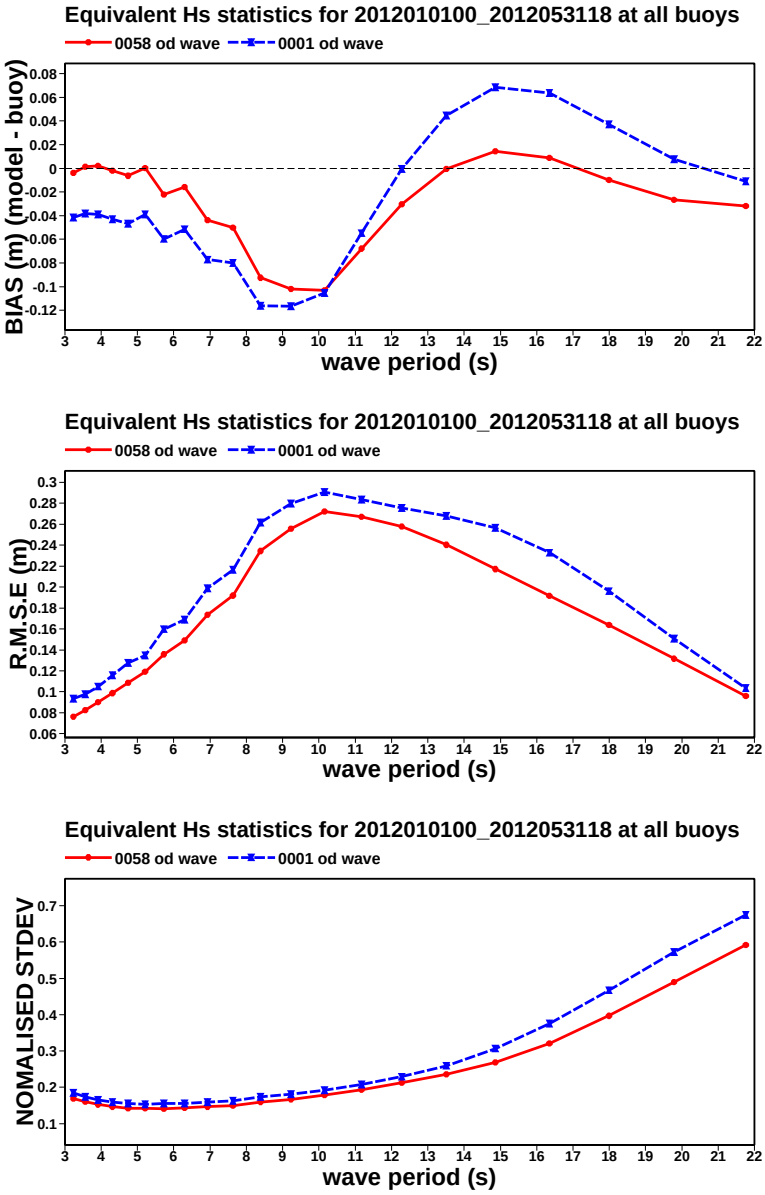


*Figure 8: Comparison of high resolution global wave analysis (28 km) with 1d spectra from buoys for the then operational system (blue 0001) and the new system in pre-operational testing (red 0058), in terms of bias (model - observations), scatter index, and correlation coefficient. The spectral data were smoothed by averaging over 3 consecutive wave model frequency bins and by converting the average energy density to equivalent wave heights. The different statistics are then plotted in terms of the corresponding wave period of each wave model frequency bin at mid point. Data are from NDBC and CDIP in the US and ISDM in Canada.*

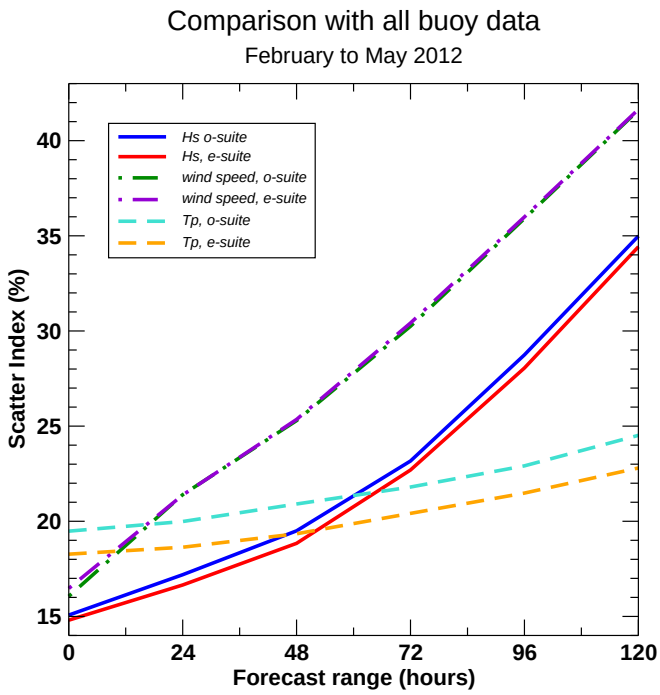


*Figure 9: Comparison of high resolution global wave forecasts with all available buoy data for the then operational system (o-suite) and the new system in pre-operational testing (e-suite).*

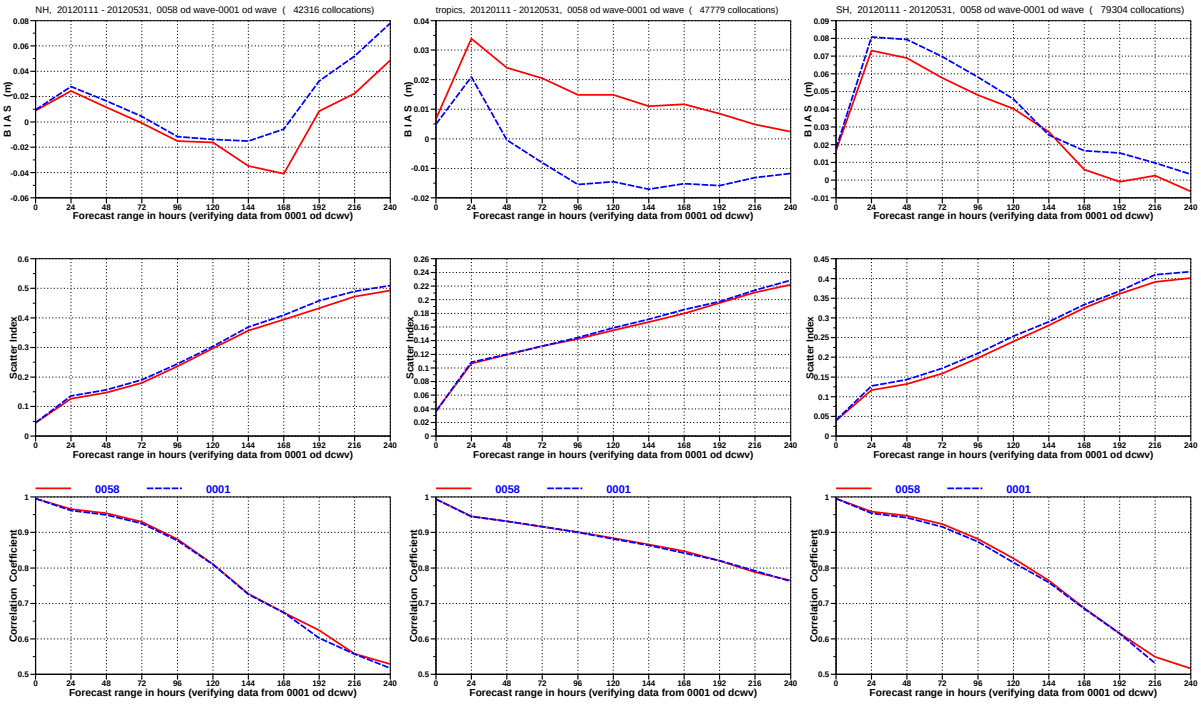


(a) Northern Hemisphere (b) Tropics (c) Southern Hemisphere

*Figure 10: Comparison of high resolution global wave forecasts with altimeter wave height data for the then operational system (blue 0001) and the new system in pre-operational testing (red 0058), in terms of bias (model - observations), scatter index, and correlation coefficient. Altimeter data are from ENVISAT and Jason 2.*

Bidlot J.-R., P. Janssen, and S. Abdalla, 2007. A revised formulation of ocean wave dissipation and its model impact. ECMWF Tech. Memo. 509. ECMWF, Reading, United Kingdom, 27pp. Available online at: http://www.ecmwf.int/publications/

Bidlot J.-R., J.-G. Li, P. Wittmann, M. Faucher, H. Chen, J.-M, Lefevre, T. Bruns, D. Greenslade, F. Ardhuin, N. Kohno, S. Park and M. Gomez, 2007: Inter-Comparison of Operational Wave Forecasting Systems. Proc. 10th International Workshop on Wave Hindcasting and Forecasting and Coastal Hazard Symposium, North Shore, Oahu, Hawaii, November 11-16, 2007. http://www.waveworkshop.org/10thWaves/ProgramFrameset.htm

Doyle J., P. Black, C. Amerault, S. Chen, and S. Wang, 2012. Wind-Wave Interactions under Hurricane Conditions: A Decade of Progress. Proceeding from the ECMWF Workshop on Ocean Waves, 25-27 June 2012.

Hardy, T., L. Mason, and L. McConochie, 2001. A wave generation model for the Great Barrier Reef. *Ocean Engineering*, **28**, 4570.

Hersbach, H. and P.A.E.M. Janssen, 1999. Improvement of the Short-Fetch Behavior in the Wave Ocean Model (WAM). *J. Atmos. Oceanic. Technol.*, **16**, 884892.

Holthuijsen, L. H., M. D. Powell, and J. D. Pietrzak, 2012. Wind and waves in extreme hurricanes. *J. Geophys. Res.*, **117**, C09003, doi:10.1029/2012JC007983.

Komen, G.J., L. Cavaleri, M. Donelan, K. Hasselmann, S. Hasselmann, and P.A.E.M. Janssen, 1994: *Dynamics and Modelling of Ocean Waves*. Cambridge University Press, 554pp.

Janssen, Peter A. E. M., 1991. Quasi-linear Theory of Wind-Wave Generation Applied to Wave Forecasting. *J. Phys. Oceanogr.*, **21**, 16311642.

Janssen, P. 2004: *The Interaction of Ocean Waves and Wind*. Cambridge University Press, 300pp.

Janssen, P. A. E. M. and Onorato, M., 2007. The intermediate water depth limit of the zakharov equation and consequences for wave prediction. *J. Phys. Oceanogr.*, **37**, 23892400.

Panofsky, H., H. Tennekes, D. Lenschow, and J. Wyngaard, 1977. The characteristics of turbulent velocity components in the surface layer under convective conditions *Boundary-Layer Meteorology*, **11**, 3, 355-361. Doi: 10.1007/BF02186086

Tolman, H. L., 2003. Treatment of unresolved islands and ice in wind wave models. *Ocean Modelling*, **5**, 219-231.